PNAS RESEARCH ARTICLE | APPLIED BIOLOGICAL SCIENCES
APPLIED PHYSICAL SCIENCES

Dielectric levitation optical tweezers for powerful mesoscale biomanipulation

Haobing Liu[a,b], Rongxin Fu[b,c,d,1], Fan Nan[e], Zongliang Guo[f], Menglei Zhao[a,b], Yifan Zhang[g], Shutong Guo[h], Hang Li[b,c,d], Kangfu Chen[d,f], Bing Chu[i], Kai Lou[i], H. P. Zhang[h], Huikai Xie[d,f], Zhugen Yang[j], Jiafang Li[k], Jonathan M. Cooper[l], and Shuailong Zhang[b,d,f,1]

Affiliations are included on p. 11.

Edited by David A. Weitz, Harvard University, Cambridge, MA; received November 18, 2025; accepted June 7, 2026

Optical tweezers (OT), a cornerstone of micromanipulation, are fundamentally constrained by substrate-induced adhesion and friction, limiting their application to mesoscale objects and fragile biological specimens where overcoming these resistive forces requires physiologically damaging laser powers. Here, we overcome this long-standing challenge by introducing dielectric levitation optical tweezers (DL-OT), a multiphysics platform that seamlessly integrates alternating-current dielectric levitation with optical traps. By using negative dielectrophoresis (n-DEP) to actively neutralize the normal force, DL-OT eliminates solid–solid contact and near-wall viscous drag. Crucially, we demonstrate the fundamental superiority of this active physical levitation over traditional passive antiadhesion coatings. This physical decoupling enables the smooth translation of large biological samples using low, biologically safe optical powers (~15 mW) rather than nonviable levels (>150 mW). The creation of this frictionless environment not only boosts the maximum manipulation speed of standard microtargets by 40% but also enables the stable optical transport of previously intractable mesoscale objects (100 to 260 μm), including microgears and shrimp eggs. By preventing photothermal damage and mechanical deformation, DL-OT demonstrates very good biocompatibility, significantly enhancing cell viability postmanipulation. Building upon these advantages, we demonstrate advanced on-chip biofabrication protocols through the targeted, high-precision assembly of multicellular spheroids and the safe transport of patient-derived organoids, followed by their success in situ culture. By transforming OT from a microscale tool into a mesoscale assembly platform, DL-OT paves the way for breakthroughs in tissue engineering, regenerative medicine, and the bottom–up assembly of living systems.

optical tweezers | dielectric levitation | micromanipulation | organoid assembly | optical trapping

Significance

Optical tweezers (OT) are a cornerstone of precision manipulation but are limited by phototoxic heat damage and surface adhesion when handling larger biological structures. These constraints have sidelined the technology in large-scale biofabrication. Here, we introduce dielectric levitation optical tweezers (DL-OT), which achieves "electro-optical synergy" by integrating light with a gentle AC electric field. This platform levitates objects to eliminate friction, expanding the manipulable size range 25-fold and doubling cell viability. By enabling the gentle, bottom–up assembly of complex, patient-derived organoids, DL-OT bridges the gap between single-cell manipulation and tissue engineering, offering a toolbox for the fabrication of functional, multiscale biological systems.

Since their introduction by Ashkin in the 1970s (1, 2), optical tweezers, a groundbreaking technology recognized with the 2018 Nobel Prize in Physics, have been widely applied in single-molecule and single-cell biophysics, mechanobiology, nanoscale assembly, and various other research fields (3, 4). Compared with other micro–nano manipulation techniques (5–8), OT stand out for their noninvasiveness, high precision, and ideal biomechanical compatibility, allowing researchers to probe the forces and dynamics governing life at its smallest scales (9, 10).

However, when manipulating particles adhered to rigid substrates or objects larger than several tens of micrometers, conventional OT face fundamental limitations. At small scales, adhesive and frictional forces, which are dominated by van der Waals interactions, electrostatic attraction, and capillary effects, can exceed the maximum optical gradient force, preventing target detachment (11–18). Large or irregularly shaped objects experience increased viscous drag and stiction, making controlled movement challenging. Overcoming these resistive forces typically requires higher laser power, which not only increases photothermal stress but also compromises the viability of delicate biological samples, such as primary cells or tissue constructs (19–21). Consequently, the manipulation range of OT has been confined to 1 to 10 μm dielectric particles, limiting their integration into mesoscale biomanufacturing tasks (22), such as organoid assembly (23), and multicellular spheroid construction (24).

Various strategies have been developed to mitigate adhesion and frictional resistance in OT manipulation. Traditional approaches often have relied on passive antiadhesion surface modifications (e.g., PEG or Teflon coatings), although their long-term efficacy is fundamentally limited by progressive protein adsorption and biofouling (25). Structural innovations—such as 3D untethered microrobots capable of out-of-plane rotation (26), slippery all-siloxane bottlebrush architectures (27), and micro Janus particles (28)—reduce surface contact and thus lower stiction. Optical field engineering, including photothermal-shock

Author contributions: H. Liu, R.F., F.N., Z.G., Y.Z., H. Li, K.C., H.P.Z., H.X., Z.Y., J.L., J.M.C., and S.Z. designed research; H. Liu, R.F., F.N., M.Z., S.G., H. Li, and H.P.Z. performed research; H. Liu, R.F., F.N., Z.G., M.Z., S.G., B.C., and K.L. contributed new reagents/analytic tools; H. Liu and R.F. analyzed data; and H. Liu, R.F., Z.G., J.M.C., and S.Z. wrote the paper.

Competing interest statement: S.Z., H. Liu, R.F., Z.G. and H. Li submitted a Chinese patent on technologies related to methodology reported in this work (CN 202411006659.8). S.Z., H. Liu, M.Z., R.F., H. Li and Z.G. granted a Chinese patent on technologies related to methodology reported in this work (CN 202411475226.7).

This article is a PNAS Direct Submission.

[1]To whom correspondence may be addressed. Email: furongxin@bit.edu.cn or shuailong.zhang@bit.edu.cn.

This article contains supporting information online at https://www.pnas.org/lookup/suppl/doi:10.1073/pnas.2533103123/-/DCSupplemental.

Published July 14, 2026.

tweezers driven by pulsed lasers (29) and resonator-based nanophotonic standing-wave array traps (30), can enhance trapping forces. To limit photothermal damage, approaches like selecting objectives with optimized numerical apertures, reducing trap-to-particle distance, employing wavelengths with low absorption (12, 31), and minimizing laser power and exposure time (32) have been implemented.

Emerging alternative low-power techniques, for example, opto-thermoelectric nanotweezers generating thermoelectric fields via thermoplasmonic substrates (33), hypothermal opto-thermophoretic tweezers (HOTT) employing environmental cooling (34), and opto-refrigerative tweezers based on solid-state optical refrigeration (35), offer further improvements in thermal management. Beyond these optical-only strategies, integrating optics with other physical or chemical fields like chemistry (36), electrochemistry (37, 38), electrokinetic (39, 40), has also demonstrated improved trapping performance. While effective in specific contexts, these methods often require complex nanofabrication, impose stringent material constraints, or lack scalability across particle sizes and morphologies. Phototoxicity and thermal stress to cells and biomolecules remain significant challenges (12, 41). An ideal, universally adaptable approach would fundamentally eliminate substrate-induced resistance, lower optical power requirements, and expand manipulation capabilities from the microscale to the mesoscale, while preserving the spatial precision and configurability of OT.

Here, we present dielectric levitation optical tweezers (DL-OT), a multiphysics platform that integrates alternating-current (AC) dielectric levitation with OT to achieve frictionless, biocompatible manipulation over a previously not-possible range of particle sizes. Inspired by magnetic levitation, DL-OT employs negative dielectrophoresis (n-DEP) within a microfluidic chamber to lift dielectric particles away from the substrate, thereby eliminating adhesion and static friction while greatly reducing near-wall viscous drag. This physical decoupling of the particle and the wall allows OT to operate effectively at much lower optical powers, minimizing photothermal stress and preserving the physiological functions of sensitive biological samples.

Using a custom-designed chip to apply the AC field during optical trapping, we simulated the electric field forces on polystyrene (PS) particles of various diameters, predicted their levitation heights, and experimentally validated these results. Moreover, DL-OT enabled the controlled manipulation of large objects, 100-μm PS microspheres and 200-μm microgears, which could not be moved by OT alone. Biocompatibility assessments with HeLa, Raji, and Jurkat cells demonstrated significantly higher postculture viability under DL-OT than with standard OT, even under limited laser power.

Importantly, in order to validate the significant improvements of active physical levitation over traditional surface modification strategies, we systematically compared DL-OT against passive antiadhesion coatings (e.g., PEG and Teflon). While passive interfaces can temporarily mitigate biofouling, they inevitably degrade during extended operation, due to progressive protein adsorption. Furthermore, forcibly dragging mesoscale objects across coated substrates still requires overcoming a high static friction threshold, which typically necessitates physiologically damaging laser powers (>150 mW) and may induce severe mechanical deformation. In contrast, by actively neutralizing the normal force and eliminating solid–solid contact, DL-OT completely bypasses this adhesion threshold. This enables the smooth, continuous translation of large biological samples using extremely low, biologically safe optical powers (~15 mW), yielding significant improvements in long-term trapping stability and geometric integrity.

Beyond overcoming the absolute immobility of massive samples, DL-OT also enhances hydrodynamic efficiency for smaller targets. Quantitative comparisons revealed that DL-OT increased the manipulation speed of 5 to 20 μm PS microspheres and yeast cells by up to 40% compared with conventional OT. Furthermore, DL-OT successfully manipulated and hatched live brine shrimp eggs (~260 μm), highlighting its capability for handling fragile mesoscale biological constructs. Such capabilities extend to on-chip bioassembly, enabling the precise positioning and integration of large, delicate structures without compromising viability. In organoid research, DL-OT could facilitate spatially controlled fusion of heterogeneous cell aggregates (42), targeted embedding of vascular structures (43), and dynamic reconfiguration of tissue models (44), thereby advancing applications in disease modeling, regenerative medicine, and personalized drug screening.

By overcoming long-standing size and adhesion barriers in optical manipulation, DL-OT provides a versatile, scalable, and biocompatible platform that bridges the gap between single-cell manipulation and tissue-level engineering. This is demonstrated through the successful assembly of multicellular clusters and the gentle manipulation of patient-derived organoids, which were subsequently cultured in situ to verify their viability. This platform offers a foundation for next-generation lab-on-a-chip systems, high-throughput organoid assembly, and in situ construction of living systems with single-cell precision.

1. Results

To provide a clear and logical framework for this study, our findings are presented in five progressive stages, transitioning from theoretical physics to mesoscopic biological applications.

Fig. 1 provides a schematic overview illustrating the fundamental scientific problem and the core innovation of our work. Fig. 2 establishes the theoretical framework, utilizing the Maxwell stress tensor method alongside multiphysics simulations to predict levitation dynamics and optimize opto-electric parameters. Fig. 3 demonstrates the broad technical feasibility of the DL-OT platform through the successful manipulation of microgears, large-scale particles, and single cells. Fig. 4 presents a comprehensive performance comparison between the DL-OT method and traditional OT using simple antiadhesion coatings, systematically highlighting the technical superiority of our approach in terms of long-term manipulation stability, minimum required optical power, manipulation velocity, and overall biosafety. Fig. 5 validates the robust manipulation capabilities of the DL-OT method on mesoscopic biological specimens, specifically utilizing brine shrimp eggs and multicellular spheroids.

A fundamental limitation of conventional OT is that the optical gradient force is often insufficient to overcome the strong surface-induced resistance (friction, adhesion, and near-wall drag) exerted on mesoscale particles in contact with a rigid substrate. As shown in Fig. 1*A*, we illustrate this physical mechanism in detail through a schematic of force decomposition. Inspired by magnetic levitation, we proposed an optical micromanipulation method that levitates particles from the substrate, decoupling z-axis and xy-axis manipulation and modifying the force balance governing motion, buoyancy, and gravity, so enabling the scaling of optical manipulation from microscale (1 to 10 μm) to mesoscale (>100 μm).We propose that our innovative approach is a methodological framework involving integration of multiphysics fields that provides a fundamental physical distinction between passive and active field decoupling. This enables active physical levitation, eliminating solid–solid contact (e.g., cell-surface), removing static friction, and reducing the normal force to near zero, thus offering a step-change advantage in fundamental performance.

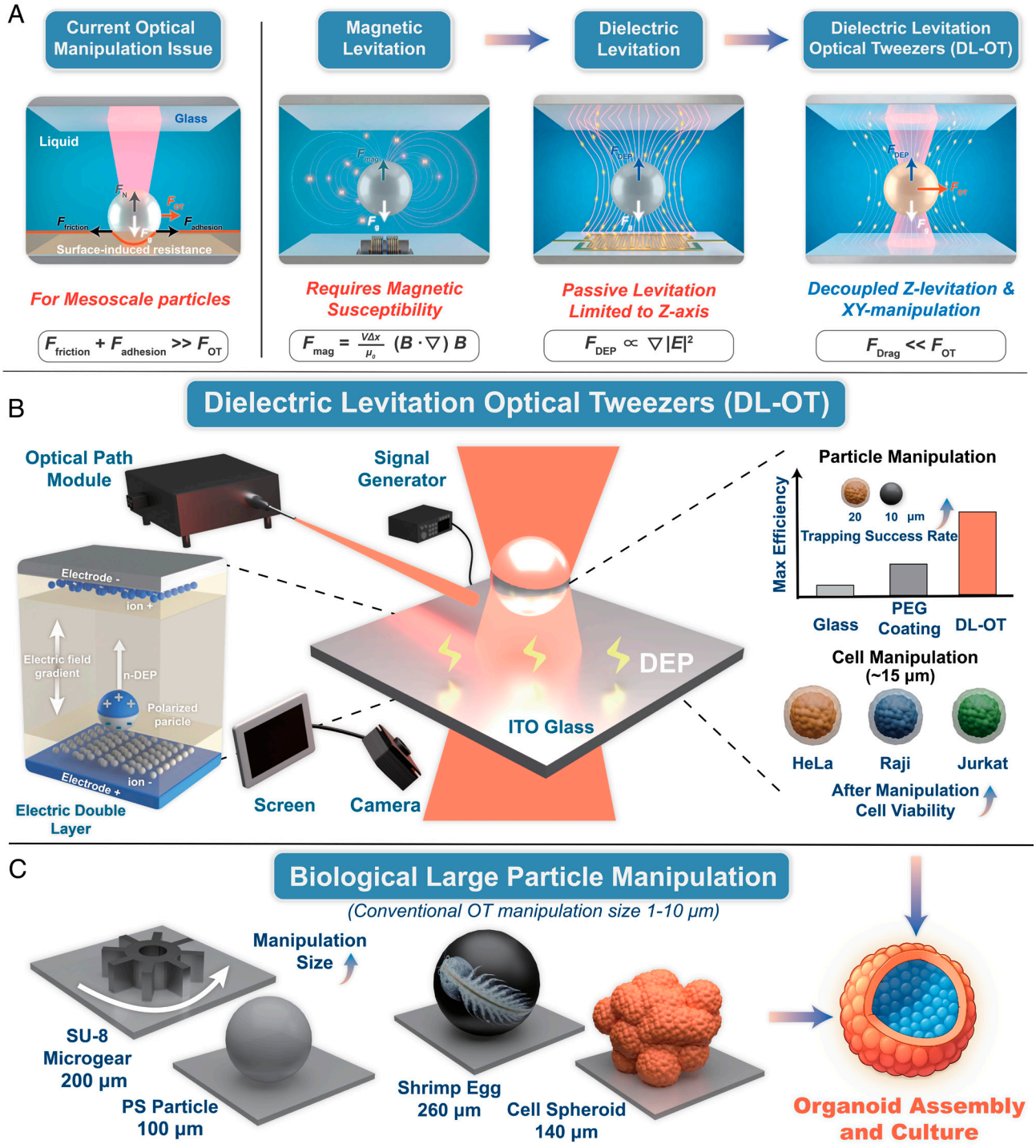

Fig. 1. Schematic of DL-OT. (*A*) Current optical manipulation issue and the inspiration. Panels 2 and 3 highlight a comparison with other techniques used to overcome the issue displayed in the first panel. Panel 4 represents the technique used in this work. (*B*) Schematic of the DL-OT system. The *Left* panel illustrates the n-DEP mechanism within the electric double layer. The *Middle* panel shows the integrated experimental setup. The *Right* panel quantitatively highlights the performance leaps of DL-OT. (*C*) Demonstration of mesoscale manipulation capabilities, overcoming the conventional 1 to 10 μm limit to stably transport large objects (100 to 260 μm), including SU-8 microgears, PS particles, shrimp eggs, and cell clusters, enabling advanced organoid assembly and culture.

The principle of DL-OT is illustrated in Fig. 1*B*. Here, dielectric particles are polarized by the applied electric field and levitated by the resulting n-DEP within the electric double layer, as depicted in the left panel. The middle panel shows a schematic of the integrated experimental setup, with a detailed configuration provided in *SI Appendix*, Figs. S1 and S2. Particles are loaded onto a custom-designed microfluidic chip, which is mounted on an inverted microscope stage using a custom fixture (*SI Appendix*, Fig. S3). This chip's main body (*SI Appendix*, Figs. S3 *A* and *B*) consists of two indium tin oxide (ITO)-coated glass plates arranged in a staggered configuration. The space between these plates is filled with the liquid medium to form a microchamber for optical manipulation (*SI Appendix*, Figs. S3 *C* and *D*). During experiments, images from within the microchamber are captured in real-time by a CMOS camera for processing and visualization.

As quantitatively highlighted in the *Right* panel of Fig. 1*B*, DL-OT offers significant fundamental advantages over both conventional OT and passive surface modification strategies.

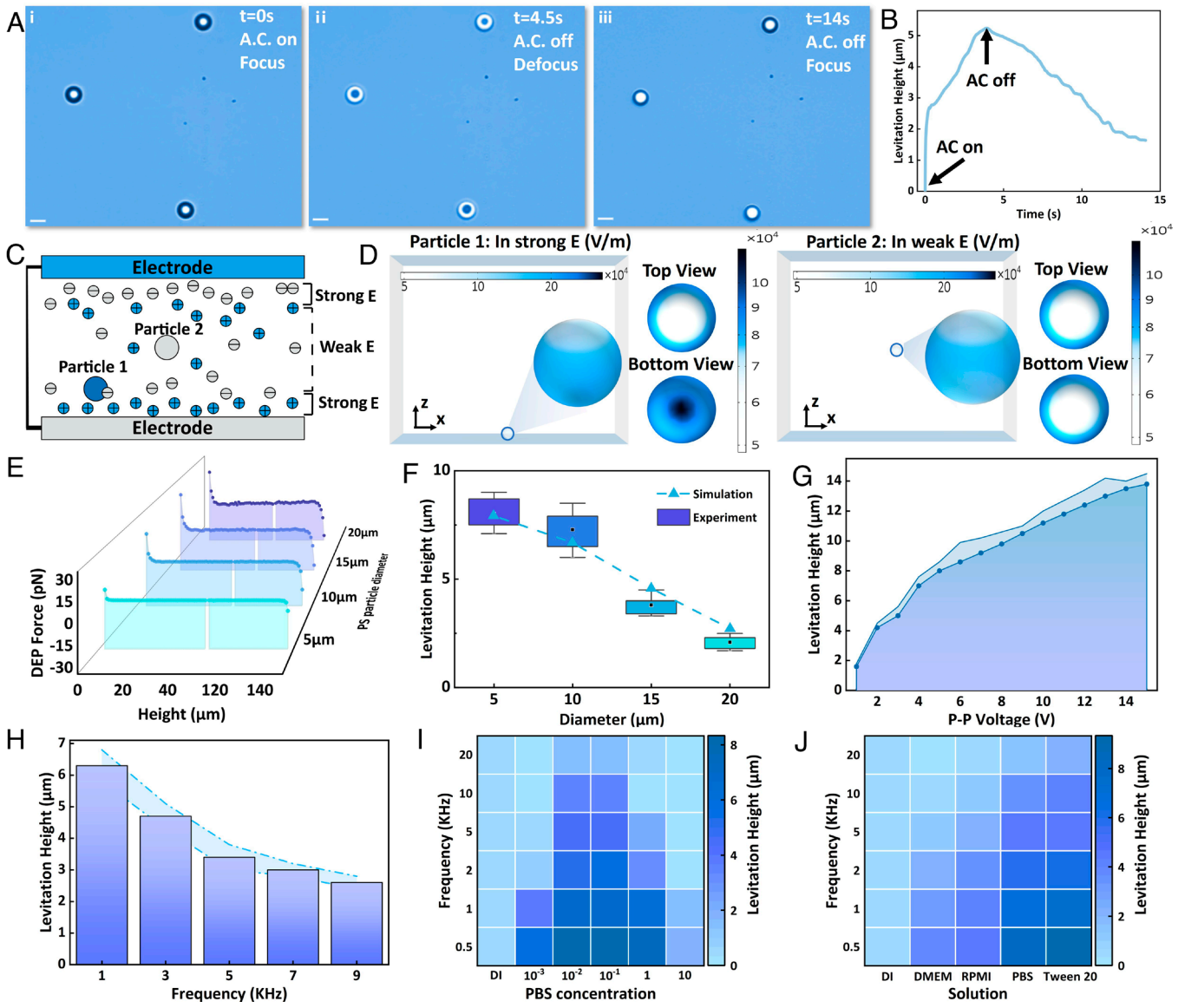

Fig. 2. Experimental and simulated characterization of the dielectric levitation mechanism in PS microspheres (*A*) Levitation and deposition process of three PS microspheres. (Scale bar, 10 μm.) (*B*) Levitation height versus time for the three PS microspheres. (*C*) Schematic of electrode polarization in the electric field, with Particle 1 located near the electrode and Particle 2 positioned farther away. (*D*) Simulated electric field strength distribution for two 10 μm PS particles under strong and weak field conditions. Insets display the isometric perspective along with the top and bottom views of the particles. The color bar represents the electric field modulus. (*E*) Simulated DEP forces for four PS microparticle sizes, highlighting heights near the top and bottom electrodes. (*F*) Experimentally measured and simulated levitation heights for four particle sizes. All simulations and experiments were conducted using a 1 kHz, 10 Vpp sinusoidal signal. The spacing between the bottom and top plates was 150 μm. (*G*) Relationship between peak-to-peak voltage and particle levitation height. Color band indicates the error bar. (*H*) Relationship between frequency and particle levitation height. Color band indicates the error bar. (*I*) Heat map of particle levitation height versus PBS concentration across the frequency range. (*J*) Heat map of particle levitation height for different solution types across the frequency range.

First, by actively eliminating solid–solid contact, DL-OT achieves significant long-term manipulation stability, demonstrating a 100% improvement in the trapping success rate for PS microspheres and a remarkable 350% improvement for biological cells compared to passive PEG coatings. Furthermore, when manipulating diverse biological samples (e.g., HeLa, Raji, and Jurkat cells), our system yielded a 124% enhancement in postmanipulation cell viability. Most importantly, DL-OT substantially extends the size limit of optically manipulated targets from the conventional 1 to 10 μm range to an unprecedented mesoscale regime (up to 260 μm), as shown in Fig. 1*C*. This breakthrough enables the precise optical transport and assembly of large-scale biological structures, including multicellular spheroids and organoids.

1.1. AC Dielectric Levitation Mechanism. We first characterized the dielectric levitation phenomenon of PS particles using our experimental setup as shown in Fig. 2*A* and Movie S1. Initially, with no electric field applied, the PS microspheres rest on the bottom substrate and appear sharply in focus (Fig. 2 *A, i*). In Fig. 2 *A, ii*, upon activation of the AC electric field, the particles levitate upward, moving out of the fixed focal plane and becoming defocused. Deactivating the field allows the particles to settle back onto the substrate under gravity, bringing them back into focus. The temporal profile of the levitation height was quantified and is plotted in Fig. 2*B*. These results were obtained by analyzing the video frames with a custom image-processing algorithm, with details provided in the Methods section and *SI Appendix*, Fig. S4. The plot shows a rapid ascent as the n-DEP force repels

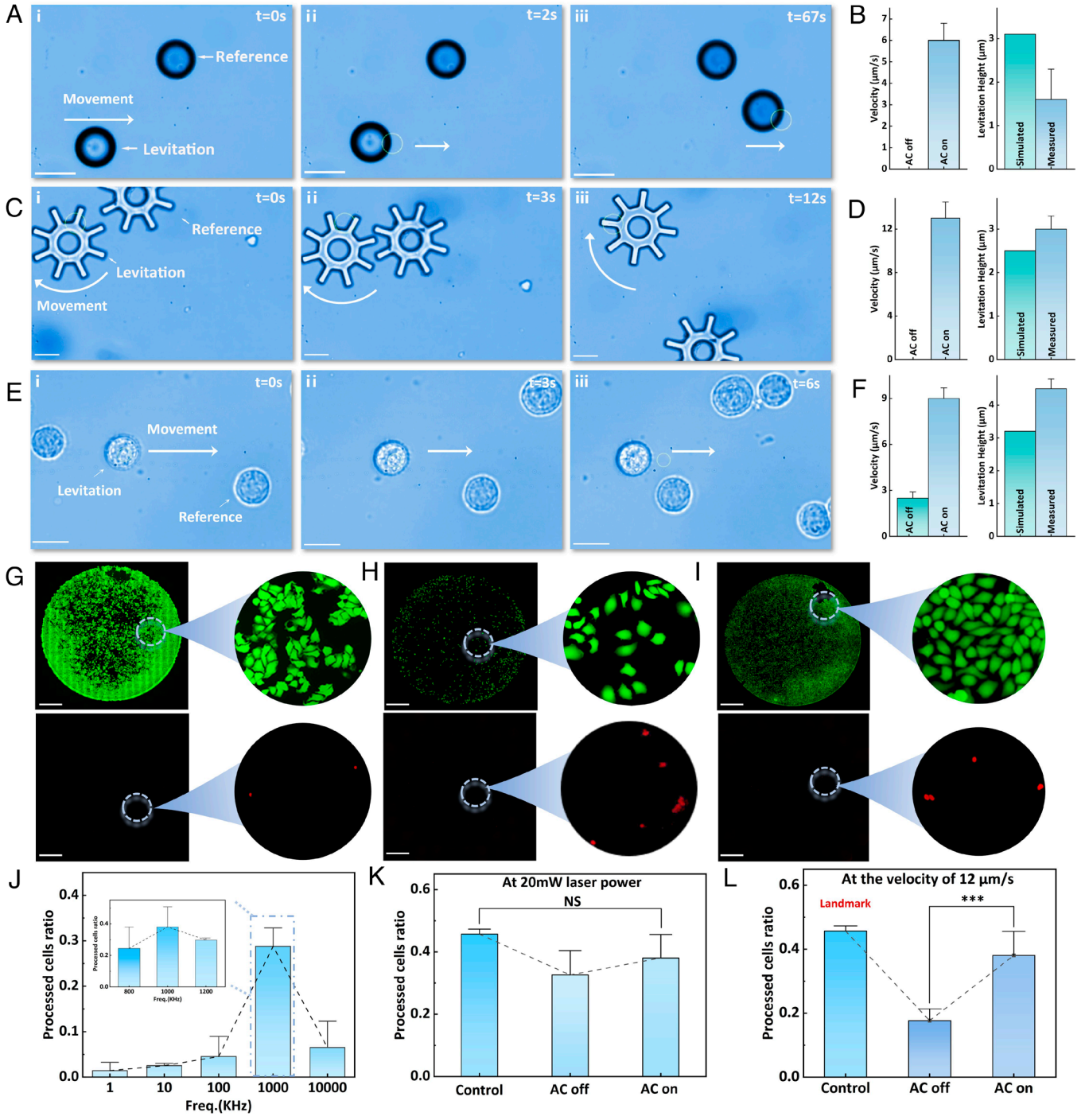

Fig. 3. Manipulation of large-sized particles and cells using DL-OT. (*A*) Movement of a levitated 100 μm PS microsphere past the reference. (Scale bar, 100 μm.) (*B*) *Left*: comparison of particle movement speed with AC on and off. *Right*: comparison of simulated and measured particle levitation heights. (*C*) Circular motion of a levitated microgear centered on a reference. (Scale bar, 100 μm.) (*D*) *Left*: comparison of gear movement speed with AC on and off. *Right*: comparison of simulated and measured gear levitation heights. (*E*) Movement of a levitated 20 μm HeLa cell past the reference. (Scale bar, 20 μm.) (*F*) *Left*: comparison of cell movement speed with AC on and off. *Right*: comparison of simulated and measured cell levitation heights. (*G*) Fluorescence images of HeLa cells with no optical manipulation. The cells were stained using Calcein-AM/PI. The image on the *Right* shows a zoom-in of the area circled by the dotted line. (Scale bar, 1 mm.) In the fluorescence images, green fluorescence indicates live cells, while red fluorescence indicates dead cells. (*H*) Fluorescence images of HeLa cells after manipulation by regular OT. (*I*) Fluorescence images of HeLa cells after manipulation by OT with AC dielectric levitation. (*J*) Relationship between cell viability and AC frequency. The "process cells ratio" denotes the ratio of fluorescent pixels to all pixels in an image. Highlights the frequency range of 800 to 1,200 kHz. (*K*) At 20 mW laser power, the viability of cells under the experimental conditions of the three groups: Control (cells with no optical manipulation), AC off (cells with optical manipulation when AC is turned off), and AC on (cells with optical manipulation when AC is turned on). NS: no significance. (*L*) At the dragging velocity of 12 μm/s, the viability of cells under the experimental conditions of the three groups. The control group is just a landmark to display the cell viability of no manipulation. ***$P < 0.001$.

the particles from the substrate, followed by a gradual descent governed by Stokes' drag and gravity once the field is removed.

Electrode polarization (EP) is the fundamental mechanism underlying AC dielectric levitation (45, 46). When an AC electric field is applied to the aqueous medium, counterions accumulate on the electrode surfaces to form an electric double layer (EDL), as depicted in Fig. 2*C*. This accumulation of ions creates an electric field strength at the electrode surface that is significantly higher than

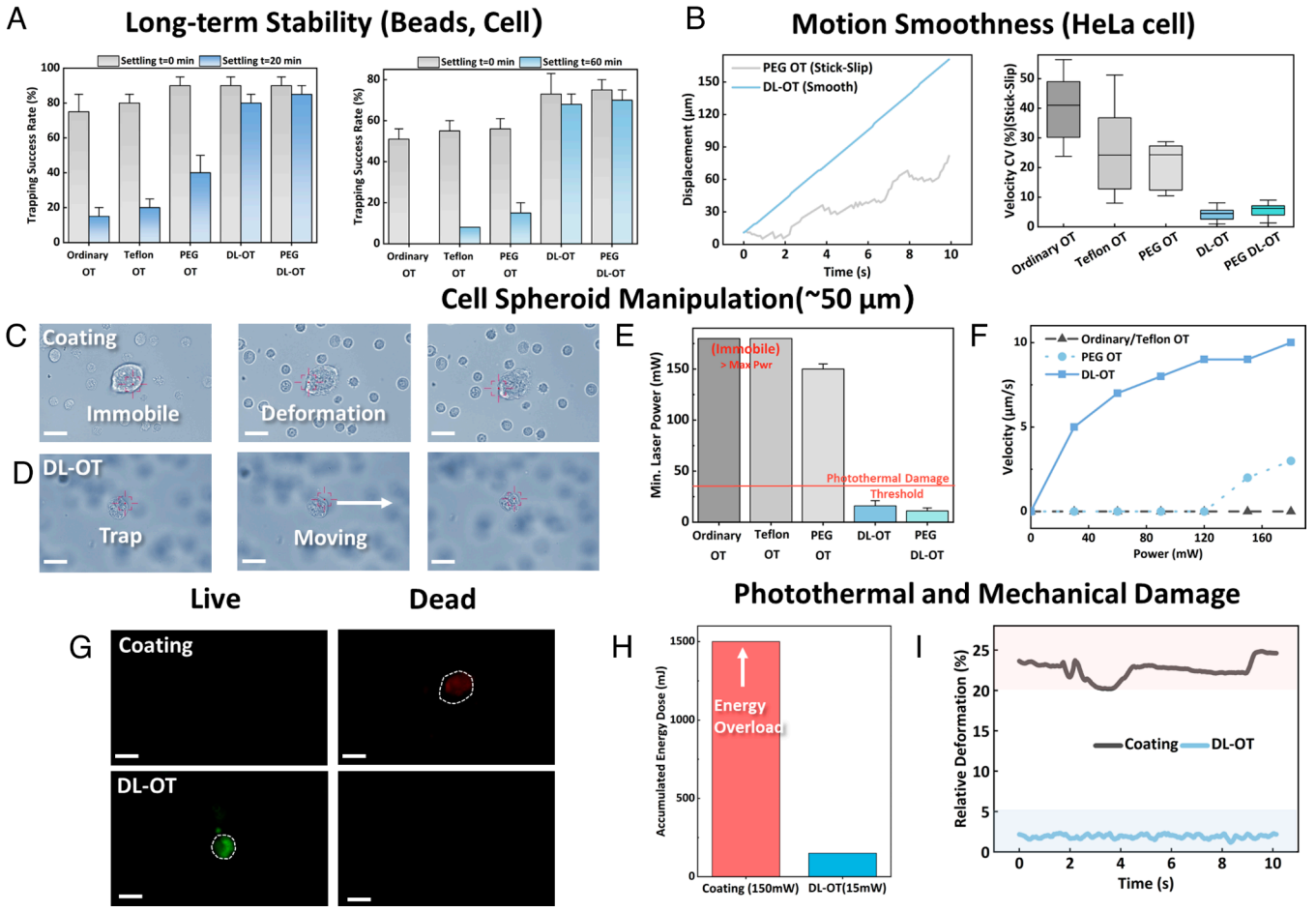

Fig. 4. Comparison of DL-OT with passive surface coatings. (*A*) Long-term trapping success rates for 10 μm PS particles (*Left*) and HeLa cells (*Right*) across different substrates. (*B*) Motion smoothness of a ~20 μm HeLa cell. *Left*: Erratic stick–slip trajectories on PEG versus smooth, linear displacement via DL-OT. *Right*: Velocity coefficient of variation (CV) highlighting the tribological stick–slip effect on coated surfaces. (*C* and *D*) Optical manipulation of a ~50 μm multicellular spheroid. (*C*) On coated surfaces, attempting to overcome static friction causes severe mechanical deformation and an immobile center of mass. (*D*) DL-OT enables intact, steady motion without structural deformation. (Scale bar, 50 μm.) (*E* and *F*) Quantitative performance for ~50 μm spheroids. (*E*) Minimum laser power required to initiate movement. Coatings necessitate physiologically lethal powers (150 mW), whereas DL-OT operates safely at 15 mW. (*F*) Corresponding velocity profiles versus laser power. (*G*) Postmanipulation live/dead fluorescence assay. The coating group (forced transport) exhibits severe phototoxicity and cell death (red, encircled), while DL-OT preserves near-perfect viability (green, encircled). (Scale bar, 50 μm.) The absence of fluorescence from the surrounding scattered single cells in the live image is due to the shallow depth of field (<1 μm) of the confocal microscope under a high-magnification oil objective, which exclusively captures the signal from the focal plane of the targeted cell spheroid. (*H*) Accumulated photothermal energy dose required for successful transport. (*I*) Relative geometric deformation of the cell spheroid when manipulating by coating OT and DL-OT.

in the bulk medium, effectively shielding the external field (47). This strong electric field gradient creates the nonuniform field required to generate a DEP force. Theoretically, given their relative permittivity (2.55 at 20 °C), much lower than that of water (80 at 20 °C), PS microspheres exhibit lower dielectric polarization than the surrounding medium. This mismatch in polarizability results in a negative DEP force. This force repels the microspheres from regions of high to low electric field strength, thereby levitating them away from the bottom electrode surface. The magnitude of the DEP force was obtained by integrating Maxwell's stress tensor over the particle surface (the limitation of the dipole approximation of DEP force is discussed in *SI Appendix*, Note S1).

$$\boldsymbol{T} = \varepsilon\left(\boldsymbol{E}\otimes\boldsymbol{E} - \frac{1}{2}E^2\boldsymbol{I}\right), \quad [1]$$

$$\boldsymbol{F}_{\mathrm{DEP}} = \oint_S T \cdot d\boldsymbol{S}, \quad [2]$$

where ε is the complex electrical permittivity, $\boldsymbol{T}$ is the Maxwell's stress tensor, $\boldsymbol{I}$ is the unit matrix, and $\boldsymbol{S}$ is the surface area of the particle.

To visualize the forces at play, we performed a finite element analysis by computationally placing particles in the strong- and weak-field regions identified in Fig. 2*C*, with the results presented in Fig. 2*D*. Full simulation parameters and procedures are available in the Methods section, *SI Appendix*, Notes S2 and Table S1 and Fig. S5. The background field distribution shows that the electric field intensity near the upper and lower electrodes is much higher than in the central region, establishing the strong vertical field gradient. Analyzing particle 1 separately, positioned near the bottom electrode, the magnified inset reveals a strong vertical electric field gradient across the particle, with a symmetrical lateral distribution. As the relative permittivity of the PS particle is lower than that of the medium, this gradient induces an upward n-DEP force. In contrast, Particle 2, located in the uniform-field region, experiences a negligible field gradient across its volume and therefore a minimal DEP force. Further simulations (Fig. 2*E*) reveal the relationship between DEP force, microsphere diameter (5, 10, 15, and 20 μm), and levitation height, obtained in point-scanning mode with a step size of 1 μm.

The simulated DEP force profiles for all particle diameters exhibit a Z-shaped trend, indicating repulsive forces from both

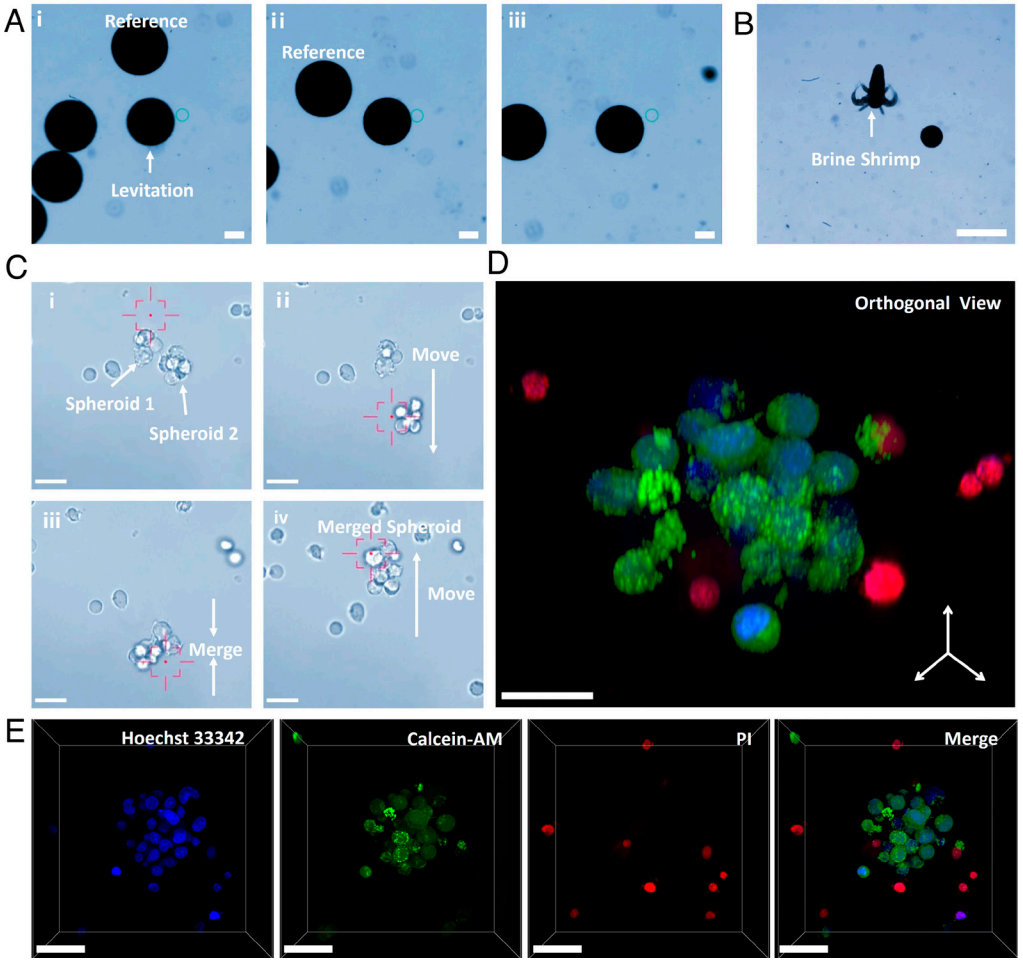

Fig. 5. Safe manipulation of biological mesoscale particles and cell spheroids. (*A*) The process of moving a 247-μm levitated brine shrimp egg. The white arrow points to a reference. The green circle marks the center position of the optical trap displayed on the software. (Scale bar, 100 μm.) (*B*) One of the hatching brine shrimps. (Scale bar, 500 μm.) (*C*) The process of moving and merging two multicellular spheroids (HL-60). (Scale bar, 50 μm.) (*D*) The orthogonal view of the confocal images of the merged spheroids cultured on-chip for 24 h. (*E*) Representative confocal images displaying three separate staining channels and the final merged image. (Scale bar, 50 μm.)

electrodes. This profile is characterized by an upward DEP force near the bottom electrode and a downward force near the top electrode, with the force approaching zero in the central region. As expected, the magnitude of the DEP force is positively correlated with particle diameter, with typical values in the piconewton (pN) range. Given this force distribution, the stable levitation height of a particle is determined by the equilibrium position where the net force—comprising the DEP force, gravity, and buoyancy—is zero. Here, the combined contribution of gravity and buoyancy represents the effective weight driven by the density difference (Δρ), as detailed in *SI Appendix*, Notes S1. The force balance is expressed as

$$\boldsymbol{F}_{net} = \boldsymbol{F}_{DEP} + \boldsymbol{F}_{W} = 0, \quad [3]$$

$$\boldsymbol{F}_{W} = \frac{4}{3}\pi r^3 \left(\rho_p - \rho_m\right) g, \quad [4]$$

where r is the particle radius, and ρ_p and ρ_m are the densities of the particle and the medium.

Solving this force-balance equation predicts that the stable levitation height of microspheres is inversely proportional to their diameter (see *SI Appendix*, Fig. S6 and Notes S3 for details). To verify this model, we validated the predicted levitation heights against experimental measurements (Fig. 2*F* and *SI Appendix*, Fig. S7). The experimental data confirm this negative correlation between levitation height and particle size and show excellent agreement with our simulation results, thus validating the accuracy of our model.

We then experimentally optimized the key parameters to achieve stable and robust particle levitation. Although levitation height increases with applied voltage, we operated at < 10 V to avoid significant Joule heating of the electrodes (Fig. 2*G*). Similarly, despite stronger n-DEP forces being generated at lower frequencies, we selected frequencies >1 kHz to prevent electrolysis of the medium (Fig. 2*H*). The ionic concentration of the solution was also a critical parameter shown in Figs. 2 *I* and *J*. Levitation performance was diminished in both low-conductivity solutions, which are insufficient to form a strong electric double layer, and in high-conductivity solutions like cell culture media, which shield the electric field. Optimal performance was achieved with 10^{-2}x to 10^{-1}x PBS buffer supplemented with Tween 20.

Notably, the contribution of the optical trap to axial confinement exhibits a distinct size dependence in the DL-OT system. For smaller particles (e.g., 5 to 10 μm), the particle's vertical position is governed by a coupled force balance between n-DEP, optical forces (gradient and scattering), and gravity/buoyancy. As detailed in *SI Appendix*, Fig. S8, activating the laser on a DEP-levitated particle induces a measurable axial displacement (defocusing effect), confirming a coupled 3D confinement where the optical trap provides a non-negligible axial restoring force. In contrast, for mesoscale objects (≥ 50 μm),

the axial optical forces become negligible compared to the substantial n-DEP and gravitational/buoyancy forces. These larger objects show negligible axial displacement during manipulation, and consequently their Z-position is fully determined by the n-DEP force balance. In this regime, the optical trap functions primarily as a lateral driving force—effectively transforming into a 2D lateral pusher that translates the object along a frictionless levitation plane, overcoming friction and drag associated with substrate interactions.

1.2. Frictionless Mesoscale Manipulation and Enhanced Biocompatibility. Leveraging this pure 2D lateral pushing mechanism, we further investigated the manipulation limits of DL-OT using two massive samples: a 100-μm PS microsphere and an SU-8 microgear with a 30-μm thickness and 200-μm diameter. The microgears are manufactured with SU-8 photoresist (48). The fabrication details and SEM images are shown in *SI Appendix*, Notes S4 and Fig. S9. These two particles were simulated using the same methods as before, with the space height increased to 300 μm to accommodate the larger dimensions. *SI Appendix*, Fig. S10*A* shows the simulation results of the electric field strength for a 100-μm microsphere and its environment. *SI Appendix*, Fig. S10*B* plots the resulting DEP force as a function of the microsphere's levitation height. *SI Appendix*, Fig. S10 *C* and *D* show the corresponding simulation results for the microgear, depicting the electric field distribution and the height-dependent DEP force, respectively. Fig. 3*A* and Movie S2 show the translational motion of a 100-μm PS microsphere, which traveled about 300 μm at an average speed of 6 μm/s, marking an improvement over the nonpowered, nonlevitated state. Fig. 3*b* shows the increase in the average particle velocity and the comparison between simulated and measured levitation heights across three tests. Fig. 3*C* and Movie S2 depict the circular motion of a levitated microgear, which, unlike the microsphere, exhibited rotational motion due to the optical trap applying force only to one edge, generating the rotational torque (49). Fig. 3*D* shows the increase in average velocity and the comparison between simulated and measured heights from three experiments. These demonstrations represent a significant advance, as manipulating objects of this scale with conventional OT is typically infeasible due to overwhelming surface forces. The heavy 100-μm microsphere, for instance, is subject to substantial substrate friction, while the microgear's large, flat surface area results in powerful adhesive forces that immobilize it. By levitating these objects, DL-OT eliminates these restrictive surface interactions. This work thus extends the utility of optical manipulation far beyond accelerating small particles, enabling the controlled transport of large and complex microstructures that were previously intractable.

Then, to demonstrate the biocompatibility and utility of our technique for life science applications, we extended our study from synthetic microspheres to living cells. HeLa cells, a type of tumor cell, are a crucial tool for scientific research in the life science community (50). The primary objective was to quantify and compare cell viability following manipulation with conventional OT versus our DL-OT system. Fig. 3*E* shows the controlled transport of a levitated 20-μm HeLa cell past the reference (Whole process shown in Movie S3). Fig. 3*F* demonstrates that with or without electric field in OT, the maximum velocity difference for HeLa cells reached 7 μm/s. Following manipulation, cell viability was assessed using a live/dead fluorescence assay, with representative images for three experimental groups shown in Figs. 3 *G–I*. The unmanipulated control group (Fig. 3*G*) exhibited robust cell growth, forming a nearly confluent monolayer after 2 d of off-chip culture. In contrast, cells manipulated with conventional OT showed a dramatic loss of viability, evidenced by a sparse population of live cells which is green fluorescence and a substantial number of dead cells which is red fluorescence (Fig. 3*H*). Crucially, cells manipulated using our DL-OT system in Fig. 3*I* displayed significantly higher viability than the conventional OT group, maintaining a healthy and dense cell population. To confirm the generality of this finding, we replicated the experiment using two suspension cell lines, Jurkat (T cell leukemia) and Raji (Burkitt's lymphoma) (51). Both cell lines showed a similar and dramatic improvement in postmanipulation viability with DL-OT compared to conventional OT, shown in *SI Appendix*, Figs. S11 and S12. The relevant content on cell culture is in *SI Appendix*, Notes S5.

Next, we established a metric based on the ratio of live-to-dead fluorescent pixels, termed the processed cells ratio (PCR) to quantitatively investigate the effect of levitation on cell viability.

$$P = \frac{N_{fluo}}{N_{fluo} + N_{non-fluo}}, \quad [5]$$

where, N_{fluo} is numbers of fluorescent pixels (live cells) and $N_{non-fluo}$ is numbers of nonfluorescent pixels(dead cells or background).

This pixel-based approach was necessary because direct cell counting via standard algorithms is unreliable at high cell densities. The metric's reliability was confirmed by validating it against two independent methods including image recognition and the cell counter, with all three showing excellent agreement in viability trends shown in *SI Appendix*, Fig. S13 *A* and *B*, separately. We then used this metric to optimize three key experimental parameters: electric field frequency, voltage, and laser power. First, to determine the optimal electric field frequency for cell viability, we performed a parameter sweep from 1 kHz to 10 MHz, guided by values reported in previous studies (52–54). This initial sweep indicated a peak in viability around 1 MHz, so two additional frequencies were tested in this region to precisely identify the optimum (Fig. 3*J*).

Based on these results, an optimal frequency of 1 MHz was selected, providing the best balance between high manipulation speed and maximal cell viability. Following a similar optimization procedure, the ideal voltage and laser power were also determined in *SI Appendix*, Fig. S13 *C* and *D*. Using these optimized parameters, we first compared cell viability at a fixed laser power of 20 mW in Fig. 3*K*. While the unmanipulated control group showed the highest viability, there was no statistically significant difference between the control and the DL-OT group, indicating that our levitation method itself does not adversely affect cell viability at moderate laser powers (55). As established previously, levitation reduces drag, meaning a lower laser power is required to achieve a given manipulation velocity. This reduction in required laser power should, in turn, lead to higher cell viability due to reduced phototoxicity. Our results confirm this hypothesis: When manipulating cells at a constant velocity of 12 μm/s, the levitated DL-OT group exhibited significantly higher viability than the nonlevitated conventional OT group (Fig. 3*L*).

1.3. Fundamental Superiority of DL-OT Over Passive Surface Coatings. To clarify the physical necessity of the DL-OT platform, we evaluated five configurations, namely: standard OT, Teflon-coated substrates, PEG-coated substrates, DL-OT, and a hybrid PEG + DL-OT method. We first quantified long-term capture success rates, finding that after 20 min, PEG-based coatings achieved a maximum success rate of only 40% (8 out of 20) for 10 μm polystyrene beads, whereas DL-OT successfully captured 80% (16 beads). This disparity became more pronounced for HeLa cells after 60 min, where the

success rate on PEG coatings plummeted to 15% compared to a robust 70% for DL-OT (Fig. 4*A*). Kinematically, when translating HeLa cells over 150 μm within 10 s, DL-OT produced a smooth, linear time-displacement trajectory indicative of continuous fluid motion, whereas the erratic, nonlinear trajectory of the PEG-OT method proved that cells remained in discontinuous contact with the substrate (Fig. 4 *B*, *Left*). Furthermore, across five independent groups (five cells per group), the coefficient of variation (CV) for maximum manipulation velocities was significantly higher for traditional OT and coating methods than for DL-OT, confirming that contact-based manipulation is highly unstable, whereas DL-OT provides reproducible motion via levitation (Fig. 4 *B*, *Right*).

We further analyzed the manipulation of ~50 μm multicellular spheroids. Time-lapse micrographs revealed that attempting to overcome static friction and biochemical adhesion on coated surfaces led to severe mechanical deformation and a stationary center-of-mass (Fig. 4*C*), whereas DL-OT enabled stable, levitated motion with negligible structural distortion (Fig. 4*D* and Movie S4). Importantly, initiating motion on coated surfaces required a physiologically lethal laser power of 150 mW, while DL-OT operated stably at a biosafe power of 15 mW (Fig. 4*E*), with corresponding velocity-power curves further validating this efficiency (Fig. 4*F*). Live/dead fluorescence assays confirmed that spheroids forcibly moved on coated surfaces suffered severe phototoxicity and extensive cell death (red), whereas those manipulated via DL-OT maintained near-perfect viability (green) (Fig. 4*G*). This is directly supported by the calculated cumulative photothermal energy dose for a 10 s transport: 1,500 mJ (150 mW × 10 s) for the coating method versus a mere 150 mJ (15 mW × 10 s) for DL-OT (Fig. 4*H*). Finally, tracking the relative shape deformation over time demonstrated that the coating group experienced significant friction-induced cellular stretching exceeding 25%, while DL-OT safely maintained deformation below 2% (Fig. 4*I*). We summarized *SI Appendix*, Table S2 to make the comparison clearer.

Beyond overcoming the absolute immobility caused by static friction, the DL-OT platform also resolves the hydrodynamic efficiency barrier for smaller, mobile targets. This highly controllable, levitation-enabled manipulation was successfully validated on small biological samples, demonstrating the stable transport of ~2 μm yeast cells (*SI Appendix*, Fig. S14). To quantify this, we extended our characterization to measure the size-dependent velocity enhancement for microspheres ranging from 5 to 20 μm (*SI Appendix*, Fig. S15). Consistent with the theoretical prediction of reduced hydrodynamic drag, DL-OT increased the maximum manipulation speed by approximately 40% across all sizes compared to conventional OT under the same laser trapping intensity. We attribute this enhancement to the particles escaping the viscous drag near-wall boundary layer, explained by Faxén. The detailed data regarding these size-dependent velocity profiles, alongside the calculation of effective near-wall viscosity based on Brownian motion analysis, have been decoupled from the friction analysis and are presented in *SI Appendix*, Fig. S15 and Notes S6.

1.4. Mesoscale Biological Manipulation and Tissue-Level Assembly. Drawn from the inspiration of Zhang. et al. (56), brine shrimp eggs—round particles with a relatively smooth surface, a certain degree of light transmittance, and an average particle size of 260 μm—were selected to test the performance and biocompatibility of our method. The diameter distribution of shrimp eggs shown in the *SI Appendix*, Fig. S16*A*. Fig. 5 *A, i–iii* shows the process of a levitated brine shrimp egg being dragged by the optical trap away from the reference. The manipulation was stable and achieved a consistent velocity (Movie S5). To perform a definitive biocompatibility test, we incubated the manipulated eggs to assess their developmental viability. The manipulated eggs successfully hatched into freely swimming nauplii (Fig. 5*B*), confirming that the procedure did not impede development. A quantitative comparison revealed no statistically significant difference in the hatching rates between the DL-OT manipulated group and an unmanipulated control group, with the variance being less than 10% in *SI Appendix*, Fig. S16*B*.

As a foundational step toward on-chip organoid engineering, we first demonstrated the controlled transport and merging of individual cell spheroids. Fig. 5*C* shows the process in which two distinct HL-60 cell spheroids, each with a maximum diameter of 50 μm, are manipulated with DL-OT and guided together, subsequently merging into a single, larger aggregate via intercellular adhesion. (Movie S6 recorded its entire process) The resulting aggregates were cultured in situ for 24 h. (Details see the *SI Appendix*, Notes S5) The confocal microscopy image (Fig. 5*D*) confirmed their three-dimensional structure and high viability via live/dead staining (Fig. 5*E*). In addition, long-term in situ culture for up to three days was successful, resulting in continued growth and a significant increase in the size of the assembled spheroids (*SI Appendix*, Fig. S17). Building on this assembly capability, we then demonstrated the gentle manipulation of a fully formed, large-scale organoid (~140 μm in diameter), using DL-OT (*SI Appendix*, Fig. S18 and Movie S6). *SI Appendix*, Fig. S19 shows the live/dead staining results of organoids after two days of on-chip culture. This demonstrates that organoids manipulated with DL-OT have good biological activity. Together, these results establish DL-OT as a powerful and biocompatible tool for the bottom–up assembly and gentle transport of complex, three-dimensional biological structures.

2. Discussion

A well-established challenge in conventional optical manipulation is the difficulty of transporting substrate-adherent particles. Our DL-OT system addresses this limitation by employing n-DEP forces to levitate particles off the substrate, thereby eliminating restrictive surface interactions. The efficacy of this approach can be understood by considering the fundamental forces at play. At the low Reynolds numbers of this system, the optical force required to translate a particle at a constant velocity is balanced by the hydrodynamic drag force. For a spherical particle far from any surface, this drag is given by Stokes' law (57):

$$F_{optical} = F_{drag}, \quad [6]$$

$$F_{drag} = 6\pi\eta r v, \quad [7]$$

where η is the viscosity of the liquid, r and v is the radius and the velocity of the microsphere.

The calculated drag forces for levitated microspheres at their maximum observed velocities are on the order of piconewtons (*SI Appendix*, Fig. S20). Since the optical trap must generate this exact force to sustain movement, this calculation explicitly indicates that the maximum available lateral propulsive force of a conventional optical trap is strictly limited to the piconewton range (typically ~10 to 50 pN). However, for larger mesoscale objects (e.g., ~50 μm spheroids and ≥ 100 μm microgears), the physical regime is fundamentally different. In this regime, conventional OT is fundamentally incapable of achieving stable lifting or true 3D trapping. These massive objects sediment into direct contact with the substrate, resulting in a substrate-contact-limited manipulation regime. They experience gravity-induced static friction and strong nonspecific adhesion (e.g., van der Waals,

electrostatic, and solvent induced hydrophobic or hydrophilic interactions, all contributing to biofouling-mediated mechanisms). These combined surface-induced forces create a finite, immobile threshold typically on the order of 10^2–10^3 pN or higher (16, 17, 58, 59). The size of this threshold force is orders of magnitude larger than the optical trapping limit, and thus cannot be addressed by simply reducing the manipulation velocity. This significant force imbalance explains why conventional optical tools, as a fundamental shortcoming, will always fail to initiate motion for large objects, and why the active normal-force neutralization provided by n-DEP levitation is required for efficient and precise manipulation.

Our proposed DL-OT platform resolves this fundamental shortcoming of optical tweezers (OT) by transforming the system to a frictionless (contact-free) manipulation. By introducing a n-DEP force that scales with particle volume, the system can easily generate upward forces ranging from hundreds to thousands of piconewtons (e.g., 400 to 4,000 pN for large objects, supported by our simulations in *SI Appendix*, Fig. S10). These are sufficient to overcome gravity and lift the objects away from the substrate, thereby eliminating the normal force and suppressing both static friction and drag associated with the particles' interaction with the surface (60). This active levitation transitions the manipulation environment into a low-resistance state governed only by reduced viscous drag. Consequently, any initial adhesive forces threshold are entirely mitigated, allowing mesoscale samples to be smoothly manipulated with merely ~15 mW of laser power, which significantly reduces thermal stress and preserves cell viability (Fig. 4 *D* and *G*).

A second factor hindering the transport of adherent particles is the increased hydrodynamic drag near the no-slip boundary of the substrate. We quantified this effect by measuring the particle's separation-dependent translational diffusion coefficient, derived from its mean squared displacement (MSD) data (*SI Appendix*, Eq. **S9**). This near-wall diffusion can be compared to the bulk-phase diffusion coefficient given by the Stokes–Einstein relation (61):

$$D_{bulk} = \frac{K_B T}{6\pi\eta R}, \qquad [8]$$

with η the viscosity, R the radius, K_B the Boltzmann constant, and T the absolute temperature.

From these diffusion measurements, we calculated the effective viscosity experienced by the particles in *SI Appendix*, Fig. S15*C*. Combining the diffusion coefficients of the adherent and bulk regions allows estimation of the microsphere's adherent height using lubrication theory (*SI Appendix*, Notes 7 and Eqs. **S10**–**S12**) and the Faxén expression (*SI Appendix*, Eqs. **S10**, **S13**, and **S14**) as described in Refs. 58 and 59. The results are displayed in *SI Appendix*, Fig. S20. These models show that larger particles sediment closer to the substrate and consequently experience significantly greater hydrodynamic drag. This finding is critical, as it demonstrates that even in the absence of static friction and adhesion, purely hydrodynamic effects are sufficient to significantly impede manipulation. This reinforces the primary advantage of DL-OT: By levitating particles away from this high-drag, near-wall region, the system dramatically reduces the optical force required for translation.

Although this active levitation provides a clear fundamental advantage over passive substrates, our results demonstrate that the two approaches are highly complementary in practical applications. During DL-OT manipulation, samples remain stably suspended; however, during brief intervals when the AC field is deactivated, antiadhesion coatings (e.g., PEG) prevent irreversible cellular attachment to the ITO surface. Consequently, a synergistic approach combining DL-OT with a PEG coating yielded the highest long-term trapping success rates (~83% for synthetic particles and ~70% for cells), making it ideal for applications requiring extended manipulation times, such as the sequential assembly of multicellular spheroids or organoids and high-throughput biofabrication workflows.

Alongside this extended operational stability, preserving cell viability during prolonged experiments strictly requires robust thermal management. To address potential concerns regarding Joule heating from the AC electric field, we performed in situ temperature measurements within the microchamber using an embedded fine-wire thermocouple. Under representative operating conditions (10 Vpp AC field, laser illumination on), the temperature increases transiently before establishing a steady-state thermal equilibrium that balances Joule heating and heat dissipation. As detailed in *SI Appendix*, Fig. S21, measurements across solvent/media with different electrical conductivities showed that temperature increases remain controlled and consistent with the expected scaling of Joule heating. Specifically, the steady-state temperature equilibrated at ~33 °C in PBS, while in cell culture medium (DMEMsteady-state was reached at approximately 36 °C. This thermal equilibrium in DMEM lies directly within the physiological range required for mammalian cell culture, confirming that the DL-OT platform effectively dissipates heat and maintains a thermally safe microenvironment for delicate biological samples.

Ultimately, building upon this stable, low-resistance, and highly biocompatible manipulation environment, we extended the capabilities of the DL-OT platform far beyond linear transport. The rotational behavior observed in our microgear experiments underscores a fundamental and generalizable mechanism of the DL-OT platform: optically induced torque generated by an off-center force application or a spatially localized optical force coupling. This capability is broadly applicable to inherently asymmetric biological samples, such as neurons, irregular tissue fragments, or asymmetric cell clusters. These complex, nonspherical geometries naturally provide built-in "optical handles" for controlled torque generation. Because DL-OT eliminates solid–solid contact (thereby removing static friction and bioadhesion) and reduces near-wall hydrodynamic drag, it enables multi-degree-of-freedom manipulation, including simultaneous translation and rotation. Consequently, these irregular samples can be freely rotated, reoriented, and assembled with high spatial precision, facilitating the construction of complex three-dimensional configurations without the need for engineered morphological features.

3. Conclusion

In this study, we have developed and validated a multiphysics platform, DL-OT, that overcomes a fundamental limitation of conventional optical manipulation. By integrating active AC dielectric levitation with OT, our system actively neutralizes the normal force, effectively eliminating the restrictive surface forces—including nonspecific adhesion, static friction, and near-wall hydrodynamic drag—that immobilize particles in contact with a substrate. We established a robust theoretical and simulation framework, validated by experiments on PS microspheres, to precisely characterize the levitation dynamics and demonstrate a significant increase in manipulation speed.

Importantly, our comprehensive comparative analysis demonstrated the fundamental superiority of DL-OT over traditional passive antiadhesion coatings. This physical decoupling directly enables the smooth, continuous translation of massive biological samples using biologically safe optical powers (~15 mW), thereby mitigating photothermal damage and maintaining geometric integrity. This physical decoupling allowed us to extend the capabilities of optical

manipulation to previously intractable size regimes, demonstrating the controlled transport of 100-μm microspheres and the rotation of 200-μm microgears. The biocompatibility and gentle nature of this technique were rigorously confirmed through a suite of biological applications, including demonstrating significantly improved viability for multiple human cell lines, hatching manipulated brine shrimp eggs, and achieving the bottom–up assembly of multicellular spheroids alongside the safe transport of delicate patient-derived organoids. The demonstrated success across scales—from single cells to developing organisms and tissue-level constructs—establishes DL-OT as a versatile and powerful platform.

Looking forward, the principles of dielectrophoretic manipulation are also applicable to nanoscale objects, including viruses and macromolecules (60). By breaking the constraints of substrate adhesion, this fusion of optical and electrical control is poised to become an indispensable tool in the optical manipulation family, opening broad avenues in fields ranging from tissue engineering and developmental biology to single-molecule studies.

4. Materials and Methods

4.1. Experimental Setup. An OT system comprises four individual components, as shown in Fig. 1*A*, with the physical diagram presented in *SI Appendix*, Fig. S1. The optical module (Holographic Optical Tweezer, SLM-HOT) was designed by Shenzhen Kayja-Optics Technology Co. Ltd. It consists of a laser, an array system, and an optical path system. Detailed information about the optical connections is shown in *SI Appendix*, Fig. S3. The optics include beam expanders, half-wave plates, polarizing beam splitter prisms, diaphragms, reflectors, etc. The inverted microscope (Nikon ECLIPSE Ti2) was modified to connect to the optical module. The OT device is composed of two rectangular pieces of ITO-coated laminated glass placed in opposite directions, sealing with a liquid medium in between, forming a cubic microchamber. Each rectangular glass piece is 75 mm long, 25 mm wide, and 0.3 mm thick, manufactured by GULUO GLASS. Unless otherwise noted, the signal generator (Keysight 33500B) generates sinusoidal waves of 10 kHz with a peak-to-peak voltage of 1 V. The amplifier (FPA2100) then boosts the signal to 10 V peak-to-peak. We designed a chip fixture to connect the chip to the signal amplifier (shown in *SI Appendix*, Fig. S2). The computer used is a Lenovo (Think Station) P720 graphics workstation. The generation of optical traps is controlled by custom-designed software.

4.2. Preparation of Samples. The 10 μm PS microspheres were purchased from Polysciences Inc., while the 5, 15, 20, and 100 μm PS microspheres were obtained from RIGOR Science. The liquid environment in which the microspheres are suspended consists of deionized water, surfactants, or salt solutions. Two surfactants were tested: Tween20 and 90R4, both at a concentration of 0.05%. According to the experimental results, particles in the Tween20 surfactant solution could be better controlled. Two salt solutions were also tested: sodium chloride and potassium chloride. After practical verification and comparison, all experiments in this study were performed in a 0.05% Tween20 solution.

The yeast cells were sourced from commercial instant dry yeast (ANGEL YEAST CO., LTD.). Dry yeast pellets (0.5 g) were dissolved in 10 mL deionized water and shaken well with a shaker for ten minutes to dissolve them thoroughly. Images of yeast cells in the solution are shown in *SI Appendix*, Fig. S9.

The HeLa cells were cultivated under controlled conditions within a cell culture incubator maintained at 37 °C, 5% CO_2, and high humidity. The growth medium consisted of Minimum Essential Medium (MEM) supplemented with 10% fetal bovine serum (FBS), 100 μg/mL penicillin, and 100 μg/mL streptomycin (Eallbio, China). Prior to initiating experiments, cells were dissociated and resuspended in fresh complete medium. Cell concentration and viability were assessed using an automated cell counter (Countess III, Thermo Fisher Scientific). Subculturing was performed every 2 to 3 d, maintaining a density of 10^5 cells/mL/cm^2. For cell dissociation, trypsin (Eallbio, China) was used, followed by centrifugation at 800 rpm for 8 min. After aspiration of the supernatant, cells were resuspended in fresh complete medium and then subjected to a 10-fold dilution in the same medium. The culture process for Raji, Jurkat, and HL-60 cells are the same as described above, with the culture medium replaced accordingly.

Patient-derived bladder cancer tumor tissues were obtained during surgical resection, following the acquisition of written informed consent from the patient, and the full study was approved by the Biomedical Research Ethics Committee of Peking University First Hospital (Ethics Approval Number: 2025R0386-0002). The establishment and culture of organoids were performed strictly according to the protocol described (62). Briefly, fresh tumor tissues were processed, embedded in Matrigel, and cultured with specific medium to form organoid microspheres, which were used in subsequent experiments.

4.3. Numerical Simulations. A 3D finite element model was constructed using COMSOL Multiphysics version 6.2. The Electric Current module was employed to simulate the steady-state electric field characteristics of the particles in the device (e.g., electric field distribution, electric potential, etc.) (63–65). Additional details about the COMSOL simulation are provided in the *SI Appendix*, Notes S2.

4.4. Image-Based Particle Height Algorithm Using ResNet-18 Regression. To quantitatively determine the levitation height of polystyrene microspheres subjected to dielectrophoretic forces relative to the focal plane, we developed an image analysis algorithm based on a ResNet-18 convolutional neural network adapted for regression. This algorithm processes an input of 128 × 128 pixel patches centered on individual microspheres and outputs the height in micrometers. The dataset consisted of 2124 labeled images capturing particles at varying heights, partitioned into training (1698 images) and validation (426 images) sets. The model was trained for 200 epochs using the Adam optimizer with a learning rate of 1e-4. To select the optimal model for prediction, a checkpointing strategy saved the instance achieving the highest R-squared (R^2) value on the validation set. This saved model was used for all reported height predictions (66). Neural network architecture and detailed algorithm training specifications are provided in the *SI Appendix*, Fig. S4.

Data, Materials, and Software Availability. All study data are included in the article and/or supporting information. The data and codes that support the plots within this paper are available on https://github.com/Liu-Haobing/Study-data-and-codes-in-DL-OT.git (66).

ACKNOWLEDGMENTS. We acknowledge the technical support from the Biological and Medical Engineering Core Facilities of Beijing Institute of Technology, Analysis and Testing Center of Beijing Institute of Technology. We also acknowledge Professor Haixia Li for providing clinical samples following permission from the Biomedical Research Ethics Committee of Peking University First Hospital (Ethics Approval Number: 2025R0386-0002). The research was supported by the National Key R&D Program of China (Grant nos. 2024YFC3406900, 2023YFE0112400, 2022YFA1207100, and 2023YFF0721500), Young Elite Scientists Sponsorship Program by CAST (2023QNRC001), the Beijing Municipal Natural Science Foundation (Grant nos. L254083, L246030, 4242060, and 2242018), the Chongqing Municipal Natural Science Foundation (Grant nos. 2024NSCQ-MSX3784, 2024NSCQ-JQX0192, and CSTB2024NSCQ-JQX0034), Shenzhen Science and Technology Program (Grant no. KJZD20240903101359020), Open Research Fund of the State Key Laboratory of Optoelectronic Materials and Technologies (Sun Yat-sen University, Grant Nos. OEMT-2024-KF-03 and OEMT-2025-KF-09), and Open Research Fund of State Key Laboratory of Digital Medical Engineering (Southeast University, 2025-K07).

Author affiliations: [a]School of Mechatronics Engineering, Beijing Institute of Technology, Beijing 100081, China; [b]Zhengzhou Research Institute, Beijing Institute of Technology, Zhengzhou 450000, China; [c]School of Medical Technology, Beijing Institute of Technology, Beijing 100081, China; [d]Engineering Research Center of Integrated Acousto-optoelectronic Microsystems (Ministry of Education of China), Beijing Institute of Technology, Chongqing Institute of Microelectronics and Microsystems, Chongqing 400030, China; [e]Institute of Biological and Chemical Systems, Karlsruhe Institute of Technology, Eggenstein-Leopoldshafen 76344, Germany; [f]State Key Laboratory of Chips and Systems for Advanced Light Field Display, School of Integrated Circuits and Electronics, Beijing Institute of Technology, Beijing 100081, China; [g]Institute of Chemistry, Chinese Academy of Sciences, Beijing 100190, China; [h]School of Physics and Astronomy, Institute of Natural Sciences and Ministry of Education Key Laboratory in Scientific and Engineering Computing, Shanghai Jiao Tong University, Shanghai 200240, China; [i]Shenzhen Kayja-Optics Technology Co. Ltd., Shenzhen 518055, China; [j]Cranfield Water Science Institute, Cranfield University, Cranfield MK43 0AL, United Kingdom; [k]State Key Laboratory of Chips and Systems for Advanced Light Field Display, School of Optics and Photonics, Beijing Institute of Technology, Beijing 100081, China; and [l]Division of Biomedical Engineering, James Watt School of Engineering, University of Glasgow, Glasgow G12 8LT, United Kingdom

1. A. Ashkin, Acceleration and trapping of particles by radiation pressure. *Phys. Rev. Lett.* **24**, 156 (1970).
2. A. Ashkin, J. M. Dziedzic, J. E. Bjorkholm, S. Chu, Observation of a single-beam gradient force optical trap for dielectric particles. *Opt. Lett.* **11**, 288–290 (1986).
3. J. L. Killian, F. Ye, M. D. Wang, Optical tweezers: A force to be reckoned with. *Cell* **175**, 1445–1448 (2018).
4. P. J. Pauzauskie *et al.*, Optical trapping and integration of semiconductor nanowire assemblies in water. *Nat. Mater.* **5**, 97–101 (2006).
5. Y. Shi *et al.*, Adaptive opto-thermal-hydrodynamic manipulation and polymerization (AOTHMAP) for 4D colloidal patterning. *Adv. Mater.* **36**, 2412895 (2024).
6. M. A. Zaman *et al.*, Spectral tweezers: Single sample spectroscopy using optoelectronic tweezers. *Appl. Phys. Lett.* **125**, 051108 (2024).
7. M. A. Zaman, L. Hesselink, Dynamically controllable plasmonic tweezers using C-shaped nano-engravings. *Appl. Phys. Lett.* **121**, 181108 (2022).
8. J. J. Chen *et al.*, CRISPR-powered optothermal nanotweezers: Diverse bio-nanoparticle manipulation and single nucleotide identification. *Light Sci. Appl.* **12**, 273 (2023).
9. G. Zhu *et al.*, Neural stimulation and modulation with sub-cellular precision by optomechanical bio-dart. *Light: Sci. Appl.* **13**, 258 (2024).
10. X. Shan *et al.*, Optical tweezers beyond refractive index mismatch using highly doped upconversion nanoparticles. *Nat. Nanotechnol.* **16**, 531–537 (2021).
11. D. B. Phillips *et al.*, An optically actuated surface scanning probe. *Opt. Express* **20**, 29679–29693 (2012).
12. K. Dholakia, B. W. Drinkwater, M. Ritsch-Marte, Comparing acoustic and optical forces for biomedical research. *Nat. Rev. Phys.* **2**, 480–491 (2020).
13. C. L. Lin *et al.*, Multiplying optical tweezers force using a micro-lever. *Opt. Express* **19**, 20604–20609 (2011).
14. D. B. Phillips *et al.*, Shape-induced force fields in optical trapping. *Nat. Photonics* **8**, 400–405 (2014).
15. E. A. Abbondanzieri, W. J. Greenleaf, J. W. Shaevitz, R. Landick, S. M. Block, Direct observation of base-pair stepping by RNA polymerase. *Nature* **438**, 460–465 (2005).
16. H. Zeng *et al.*, Light-fueled microscopic walkers. *Adv. Mater.* **27**, 3883–3887 (2015).
17. P. H. Tsang, G. L. Li, Y. V. Brun, L. Ben Freund, J. X. Tang, Adhesion of single bacterial cells in the micronewton range. *Proc. Natl. Acad. Sci. U.S.A.* **103**, 5764–5768 (2006).
18. H. Marvi, S. Song, M. Sitti, Experimental investigation of optimal adhesion of mushroom like elastomer microfibrillar adhesives. *Langmuir* **31**, 10119–10124 (2015).
19. I. A. Favre-Bulle, A. B. Stilgoe, H. Rubinsztein-Dunlop, E. K. Scott, Optical trapping of otoliths drives vestibular behaviours in larval zebrafish. *Nat. Commun.* **8**, 630 (2017).
20. P. S. Kollipara, Z. H. Chen, Y. B. Zheng, Optical manipulation heats up: present and future of optothermal manipulation. *Acs Nano* **17**, 7051–7063 (2023).
21. J. X. Zhou *et al.*, Nanorefrigerative tweezers for optofluidic manipulation. *Appl. Phys. Lett.* **120**, 163701 (2022).
22. C. J. Bustamante, Y. R. Chemla, S. Liu, M. D. Wang, Optical tweezers in single-molecule biophysics. *Nat. Rev. Methods Primers* **1**, 25 (2021).
23. M. Natta, G. Cocchi, R. Tognato, A. Cianciosi, T. Serra, Advanced contactless bioassembly approaches: Leveraging sound, optical, and magnetic fields. *Adv. NanoBiomed Res.* **5**, 2400097 (2025).
24. S.-M. Kang, D. Kim, J.-H. Lee, S. Takayama, J. Y. Park, Engineered microsystems for spheroid and organoid studies. *Adv. Healthc. Mater.* **10**, 2001284 (2021).
25. D. Chan *et al.*, Combinatorial polyacrylamide hydrogels for preventing biofouling on implantable biosensors. *Adv. Mater.* **34**, 2109764 (2022).
26. E. Avci, M. Grammatikopoulou, G. Z. Yang, Laser-printing and 3D optical-control of untethered microrobots. *Adv. Opt. Mater.* **5**, 1700031 (2017).
27. Y. J. Gu, H. Zhou, F. H. Liu, S. X. Zhou, W. P. Wu, A fluffy all-siloxane bottlebrush architecture for liquid-like slippery surfaces. *J. Mater. Chem. A* **11**, 22167–22177 (2023).
28. G. Tkachenko, V. G. Truong, C. L. Esporlas, I. Sanskriti, S. Nic Chormaic, Evanescent field trapping and propulsion of Janus particles along optical nanofibers. *Nat. Commun.* **14**, 1691 (2023).
29. Z. Q. Gu *et al.*, Autonomous nanorobots with powerful thrust under dry solid-contact conditions by photothermal shock. *Nat. Commun.* **14**, 7663 (2023).
30. F. Ye, J. T. Inman, Y. Hong, P. M. Hall, M. D. Wang, Resonator nanophotonic standing-wave array trap for single-molecule manipulation and measurement. *Nat. Commun.* **13**, 77 (2022).
31. C. Chen *et al.*, Multi-photon near-infrared emission saturation nanoscopy using upconversion nanoparticles. *Nat. Commun.* **9**, 3290 (2018).
32. A. Blázquez-Castro, Optical tweezers: Phototoxicity and thermal stress in cells and biomolecules. *Micromachines-Basel* **10**, 507 (2019).
33. L. Lin *et al.*, Opto-thermoelectric nanotweezers. *Nat. Photonics* **12**, 195–201 (2018).
34. P. S. Kollipara *et al.*, Hypothermal opto-thermophoretic tweezers. *Nat. Commun.* **14**, 5133 (2023).
35. J. Li *et al.*, Opto-refrigerative tweezers. *Sci. Adv.* **7**, eabh1101 (2021).
36. M. Zhang *et al.*, Hydrogel muscles powering reconfigurable micro–metastructures with wide–spectrum programmability. *Nat. Mater.* **22**, 1243–1252 (2023).
37. Y. Cao *et al.*, Bipolar photoelectrochemistry for phase-modulated optoelectronic hybrid nanomotor. *J. Am. Chem. Soc.* **146**, 17931–17939 (2024).
38. Y. Gao *et al.*, Template-guided silicon micromotor assembly for enhanced cell manipulation. *Angew. Chem. Int. Ed.* **63**, e202405895 (2024).
39. A. H. Squires, Electrokinetic manipulation of a nanowire. *Nat. Nanotechnol.* **18**, 1128–1129 (2023).
40. Z. Liang, H. Joh, B. Lian, D. E. Fan, Light-stimulated micromotor swarms in an electric field with accurate spatial, temporal, and mode control. *Sci Adv.* **9**, eadi9932 (2023).
41. A. Ozcelik *et al.*, Acoustic tweezers for the life sciences. *Nature Methods* **15**, 1021–1028 (2018).
42. S. A. Yi, Y. Zhang, C. Rathnam, T. Pongkulapa, K.-B. Lee, Bioengineering approaches for the advanced organoid research. *Adv. Mater.* **33**, 2007949 (2021).
43. M. A. Skylar-Scott *et al.*, Biomanufacturing of organ-specific tissues with high cellular density and embedded vascular channels. *Sci. Adv.* **5**, eaaw2459 (2019).
44. M. E. Todhunter *et al.*, Programmed synthesis of three-dimensional tissues. *Nat. Methods* **12**, 975–981 (2015).
45. X. W. Chen, X. Chen, Y. X. Peng, L. L. Zhu, W. Wang, Dielectrophoretic colloidal levitation by electrode polarization in oscillating electric fields. *Langmuir* **39**, 6932–6945 (2023).
46. J. J. Chen *et al.*, Highly-adaptable optothermal nanotweezers for trapping, sorting, and assembling across diverse nanoparticles. *Adv. Mater.* **36**, 2309143 (2024).
47. F. D. Ma, D. T. Wu, N. Wu, Formation of colloidal molecules induced by alternating-current electric fields. *J. Am. Chem. Soc.* **135**, 7839–7842 (2013).
48. S. L. Zhang *et al.*, Reconfigurable multi-component micromachines driven by optoelectronic tweezers. *Nat. Commun.* **12**, 5349 (2021).
49. S. L. Neale, M. P. Macdonald, K. Dholakia, T. F. Krauss, All-optical control of microfluidic components using form birefringence. *Nat. Mater.* **4**, 530–533 (2005).
50. I. N. Lyapun, B. G. Andryukov, M. P. Bynina, Hela cell culture: immortal heritage of Henrietta lacks. *Mol. Genet. Microbiol. Virol.* **34**, 195–200 (2019).
51. Z. L. Guo *et al.*, Deep learning-assisted label-free parallel cell sorting with digital microfluidics. *Adv. Sci.* **12**, 2408353 (2024).
52. X. Li, F. Yang, B. Rubinsky, A correlation between electric fields that target the cell membrane potential and dividing hela cancer cell growth inhibition. *IEEE Trans. Bio-Med. Eng.* **68**, 1951–1956 (2021).
53. E. D. Kirson *et al.*, Alternating electric fields arrest cell proliferation in animal tumor models and human brain tumors. *Proc. Natl. Acad. Sci. U.S.A.* **104**, 10152–10157 (2007).
54. A. A. Aguilar *et al.*, Permeabilizing cell membranes with electric fields. *Cancers* **13**, 13092283 (2021).
55. M. P. Landry, P. M. McCall, Z. Qi, Y. R. Chemla, Characterization of photoactivated singlet oxygen damage in single-molecule optical trap experiments. *Biophys. J.* **97**, 2128–2136 (2009).
56. R. Q. Zhang *et al.*, Acoustic tweezers and motor for living cells. *Appl. Phys. Lett.* **116**, 123503 (2020).
57. S. M. Yang *et al.*, Dynamic manipulation and patterning of microparticles and cells by using TiOPc-based optoelectronic dielectrophoresis. *Opt. Lett.* **35**, 1959–1961 (2010).
58. A. J. Goldman, R. G. Cox, H. Brenner, Slow viscous motion of a sphere parallel to a plane wall. I. Motion through a quiescent fluid. *Chem. Eng. Sci.* **22**, 67 (1967).
59. M. E. Oneill, A slow motion of viscous liquid caused by a slowly moving solid sphere–An Addendum. *Mathematika* **14**, 67–74 (1967).
60. M. Viefhues, R. Eichhorn, DNA dielectrophoresis: Theory and applications a review. *Electrophoresis* **38**, 1483–1506 (2017).
61. S. Ketzetzi, J. de Graaf, D. J. Kraft, Diffusion-based height analysis reveals robust microswimmer-wall separation. *Phys. Rev. Lett.* **125**, 238001 (2020).
62. C. M. Cattaneo *et al.*, Tumor organoid–T-cell coculture systems. *Nat. Protoc.* **15**, 15–39 (2020).
63. W. Dong *et al.*, Light-programmable nanograspers for rapid nanoplastics detection in biological fluids. *ACS Nano* **20**, 9358–9370 (2026).
64. B. Xu *et al.*, Tuning self-assembled topological dipoles in optoelectronic traps. *Laser Photon. Rev.* **20**, e01697 (2026).
65. G. Li *et al.*, Crossing the dimensional divide with optoelectronic tweezers: Multicomponent light-driven micromachines with motion transfer in three dimensions. *Adv. Mater.* **37**, 2417742 (2025).
66. H. Liu *et al.*, Study-data-and-codes-in-DL-OT. GitHub. https://github.com/Liu-Haobing/Study-data-and-codes-in-DL-OT.git. Deposited 27 June 2026.